Journal of Fluids and Structures (2000) **14,** 127–146
doi: 10.1006/jfls. 1999.0257, available online at http://www.idealibrary.com on IDEAL®

COUPLED ANALYSIS OF NONLINEAR INTERACTION BETWEEN FLUID AND STRUCTURE DURING IMPACT

C. H. Lu, Y. S. He

Department of Engineering Mechanics, Shanghai Jiao Tong University Shanghai, 200030, China

AND

G. X. Wu

Department of Mechanical Engineering, University College London, Torrington Place London WC1E 7JE, U.K.

(Received 15 May 1998 and in final form 10 August 1999)

This paper presents a method for analysing the hydroelastic interaction during the impact of a structure with water. The completely coupled equation for fluid flow and structural response is solved by the boundary element method for the former and by the finite element method for the latter. During the impact, the nonlinear free surface boundary condition is satisfied, including proper treatment of the jet, and the full interaction with the linear elastic structure is taken into account. The convergence of the code is verified by different fluid domain and mesh sizes and different time steps. The accuracy of the code is confirmed by comparing the obtained results with published data. Various examples of a V-shape structure impacting vertically upon water are provided. The numerical result from this coupled analysis shows that the hydroelasticity has different effects on the dynamic response of the body with different deadrise angles, which may have some important implications for structural design.

1. INTRODUCTION

The fluid–structure impact problem is of great importance in many engineering applications. When the structure enters water at high speed, it may encounter very high hydrodynamic pressure and the structure may be damaged as a result. Cases of severe damage to ship bows due to impact have been reported (Vamammoto *et al.* 1985).

Von Karman (1929) appears to be the first to have studied the impact problem. Since his work, there has been a considerable number of publications on this problem. Most researchers used or extended Wagner's flat-plate approximation (Wagner 1932) and the work mainly concentrated on rigid bodies. There are fewer studies which deal with the hydroelastic effects on the impact. Earlier applications based on the framework of Wagner include that by Meyerhoff (1965) and by Wilkinson *et al.* (1968).

In other analyses, numerical methods have also been used for the fluid loading. Typical examples include the work by Belystchko & Mullen (1981). They studied the fluid–structure interaction for a two-dimensional cylindrical shell entering water in a short tank. The hydrodynamic problem is solved using the Navier–Stokes (N–S) equations based on the finite difference method. One of the difficulties in the analysis is that the shape of the wetted surface and the velocity distribution over it are unknown before the N–S equations are solved, which in turn depend on these unknown parameters. To overcome this, Belystchko & Mullen have used the solution from the last time step to obtain the boundary condition

0889–9746/00/010127 + 20 $35.00/0

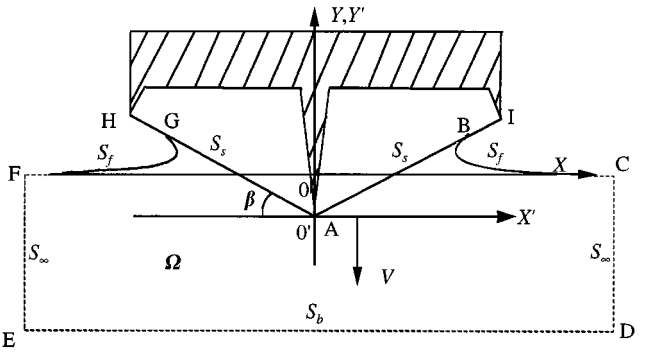

Figure 1. Definition of computational domain.

for the N–S equations on the wetted surface at the current time step. Once the hydrodynamic problem is solved, the obtained fluid loading on the wetted surface can be used as the external force for the structural response. The solution from the structural analysis will give a new boundary condition on the wetted surface for the N–S equations at the next time step. Evidently, although this method takes into account the interaction between the fluid and the body, the hydrodynamic and structural analyses are entirely separated. In fact, the technique is similar to the explicit method in the N–S equations. Although it is simple, the method is less accurate than the implicit technique and is prone to instability in the time domain.

To fully take into account the interaction between the fluid and the body through the wetted surface, it seems that iteration is inevitable. At each time step, the technique starts the hydrodynamic analysis based on the assumed shape of the wetted surface and the velocity distribution, for example, using the solution of the previous time step. The fluid loading obtained is used in the structural analysis to obtain the surface shape and the velocity distribution. If the difference between the assumed and the newly obtained value is within an acceptable error, the iteration stops; otherwise, the calculation continues. An application based on this technique has been made by Gu *et al.* (1991) when analysing a rotated cylindrical shell with flat bottom entering water vertically. Although this method is more accurate and is known to be less prone to instability in the time domain, it usually takes far more CPU.

In this paper, a method different from those discussed above is presented. The fluid flow is solved based on potential flow theory, which is known to give satisfactory results for this type of problem. The fluid loading is obtained from Bernoulli's equation. To overcome the difficulty associated with the nonlinear terms and to avoid the iterations, a scheme similar to the semi-implicit method in the N–S equations is used. Bernoulli's equation is effectively linearized by taking results for some terms from the solution obtained at the last time step. The equations for hydrodynamic and structural analyses are then combined to form a new matrix equation which is solved to provide results for both fluid flow and the structural response simultaneously. The results obtained by this technique have been compared with the solution from the iterative method. It is found that they are in excellent agreement, but the former method takes far less CPU.

In this paper, the hydrodynamic problem is solved based on the boundary element method (BEM) together with the fully nonlinear free surface condition. The structural response is analysed based on linear elastic theory using the finite element method (FEM). The full fluid–structure interaction is included in the manner described above. The jet formed along the body surface is treated by introducing an extra jet-element, similar to that

adopted by Zhao & Faltinsen (1993). However, here we also impose some condition on the jet thickness, which leads to a better simulation for the jet flow. Numerical results for a V-shaped structure impacting vertically upon water with constant speed are provided. The wave elevation and pressure distribution corresponding to the rigid body have been compared with those obtained from Zhao & Faltinsen (1993) and good agreement has been found. Extensive results are provided to show the effects of the thickness and the deadrise angle of the plate on the hydroelastic interaction.

2. THEORY

The fluid flow is assumed to be inviscid and incompressible, and gravitation is ignored. Figure 1 shows a two-dimensional elastic V-shaped structure entering the initially calm water with a vertical velocity. The origin of the global coordinate system and the x-axis are located on the undisturbed water surface. The y-axis points upwards and is the symmetry line of the structure. The structure is composed of two elastic plates, which are hinged at the joint point A and at the edge points H and I. The moving coordinate system $0'$-x'-y' in the figure is defined with x'-axis parallel to the x-axis, the y'-axis parallel to the y-axis and origin $0'$ being located at point A. As shown in Figure 1, Ω is the fluid domain, and $\partial\Omega = S_s + S_f + S_b + S_\infty$ is the fluid boundary, where S_s is the wetted surface of the structure, S_f is the free surface, S_b is the bottom and S_∞ is the boundary at infinity. L and h used in what follows denote the length and thickness of the plate on each side, respectively.

2.1. Hydrodynamic Analysis

Based on the above assumptions, the hydrodynamic analysis can be made using velocity potential flow theory. The potential ϕ satisfies the Laplace equation

$$\nabla^2\phi = 0, \quad (x, y)\in\Omega. \tag{1}$$

The kinematic condition on the free surface states that the fluid particles on the free surface will remain on the free surface at all times, namely

$$\frac{\mathrm{D}x}{\mathrm{D}t} = \frac{\partial\phi}{\partial x}, \quad \frac{\mathrm{D}y}{\mathrm{D}t} = \frac{\partial\phi}{\partial \mathrm{y}}, \quad (x, y)\in S_f. \tag{2}$$

The dynamic condition on the free surface assumes that the hydrodynamic pressure on S_f is equal to the atmospheric pressure which is taken as a constant. This leads to

$$\frac{\mathrm{D}\phi}{\mathrm{D}t} = \frac{1}{2}\left[\left(\frac{\partial\phi}{\partial x}\right)^2 + \left(\frac{\partial\phi}{\partial y}\right)^2\right], \quad (x, y)\in S_f, \tag{3}$$

where $\mathrm{D}/\mathrm{D}t$ denotes the substantial derivative with respect to time t. The rest of the boundary conditions can be written as

$$\frac{\partial\phi}{\partial n} = \begin{cases}\mathbf{V}\cdot\mathbf{n} - \dot{w} & \text{on } S_s\\ 0 & \text{on } S_\infty\cup S_b,\end{cases} \tag{4}$$

where $\mathbf{n}$ is the unit normal vector to the boundaries of the fluid domain, and its positive direction points out of the fluid domain; $\mathbf{V}$ is the velocity of the rigid motion of the body, and $\dot{w}$ is the normal velocity component of the elastic displacement of the structure, its positive direction being opposite to $\mathbf{n}$.

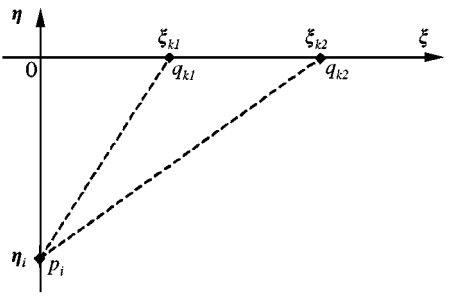

Figure 2. Local coordinate system of the kth boundary element.

The direct boundary integral method is used to solve the above potential flow problem. The boundary of the fluid domain is divided into straight-line segments (boundary elements). The values of ϕ and ϕ_n are defined at the both nodes of each element and a linear variation of ϕ and ϕ_n within the element is assumed. Thus

$$f = \left[1 - \frac{\xi - \xi_1}{l}\frac{\xi - \xi_1}{l}\right]\begin{Bmatrix} f_1 \\ f_2 \end{Bmatrix} = [N_1, N_2]\begin{Bmatrix} f_1 \\ f_2 \end{Bmatrix}, \tag{5}$$

where f can be either ϕ or ϕ_n, f_1 and f_2 are the values at the nodes, l is the length of the element, ξ_1 is the coordinate of the first point of the element along the ξ-axis defined in Figure 2. The boundary integral equation at node p can then be written as

$$\alpha\phi_p = \int_{\partial\Omega}\left(\phi_q\frac{\partial G(p,q)}{\partial n_q} - \frac{\partial\phi}{\partial n_q}G(p,q)\right)\mathrm{d}S, \tag{6}$$

where α is the solid angle of the boundary at the field point p, q is the source point on the boundary, $G(p,q) = \ln(r)$ and r is the distance between p and q. Substituting equation (5) into equation (6) leads to the following discrete equation:

$$\begin{aligned} -\alpha\phi_i + \sum_{k=1}^{N_e}\left[\left(I_{12} - \frac{\xi_{k2}}{l}I_{11}\right)\phi_{k1} + \left(\frac{\xi_{k1}}{l}I_{11} - I_{12}\right)\phi_{k2}\right] \\ = \sum_{k=1}^{N_e}\left[\left(\frac{\xi_{k2}}{2l}I_{21} - I_{22}\right)\phi_{nk1} + \left(I_{22} - \frac{\xi_{k1}}{2l}I_{21}\right)\phi_{nk2}\right], \end{aligned} \tag{7}$$

in which i corresponds to node p, N_e is the total number of nodes, k_1 and k_2 denote the first and second nodes of the kth element on the boundary. The other parameters in equation (7) are defined as

$$\begin{aligned} I_{11} &= \arctan\frac{\xi_{k2}}{\eta_i} - \arctan\frac{\xi_{k1}}{\eta_i}, \qquad I_{12} = \frac{\eta_i}{2l}\ln\frac{\eta_i^2 + \xi_{k2}^2}{\eta_i^2 + \xi_{k1}^2}, \\ I_{21} &= \xi_{k2}\ln(\eta_i^2 + \xi_{k2}^2) - \xi_{k1}\ln(\eta_i^2 + \xi_{k1}^2) - 2l + 2\eta_i I_{11}, \\ I_{22} &= \frac{1}{4l}[(\eta_i^2 + \xi_{k2}^2)\ln(\eta_i^2 + \xi_{k2}^2) - (\eta_i^2 + \xi_{k1}^2)\ln(\eta_i^2 + \xi_{k1}^2) - (\xi_{k2}^2 - \xi_{k1}^2)], \end{aligned} \tag{8}$$

where, as shown in Figure 2, p_i is the ith node of the boundary, q_{k1} and q_{k2} are the first and second nodes of the kth boundary element, the 0–ξ axis of the local coordinate system is

located on the straight line formed by the kth element, and the 0–η axis is perpendicular to the element and passes through node p_i. The positive direction of axis 0–η is the same as that of the normal vector $\mathbf{n}$. In equations (7) and (8), ξ_{k1} and ξ_{k2} are the local coordinates of nodes q_{k1} and q_{k2}, η_i is the local coordinate of node p_i, and

$$\begin{aligned} l &= \sqrt{(x_{k2} - x_{k1})^2 + (y_{k2} - y_{k1})^2}, \\ \eta_i &= [(x_{k1} - x_i)(y_{k2} - y_{k1}) - (x_{k2} - x_{k1})(y_{k1} - y_i)]/l, \\ \xi_{k1} &= [(y_{k1} - y_i)(y_{k2} - y_{k1}) + (x_{k1} - x_i)(x_{k2} - x_{k1})]/l, \\ \xi_{k2} &= [(y_{k2} - y_i)(y_{k2} - y_{k1}) + (x_{k2} - x_i)(x_{k2} - x_{k1})]/l, \end{aligned} \tag{9}$$

in which (x_i, y_i) is the global coordinate of the node p_i, and (x_{k1}, y_{k1}) and (x_{k2}, y_{k2}) are the global coordinates of the nodes q_{k1} and q_{k2}.

By rearranging equation (7), the boundary integral equation can be reduced to an algebraic equation. The following matrix equation can then be derived:

$$[H]\{\phi\} = [G]\{\phi_n\} \tag{10}$$

in which $[H]$ and $[G]$ are the coefficient matrices; they and are only functions of the geometry of the boundary of the fluid domain, and can be calculated analytically through equations (8) and (9).

After taking into account different types of boundary condition on $\partial\Omega$ and moving all the unknown variables to the left-hand side of the equation, the above matrix equation can be rewritten as

$$[H^s \;\; G^f \;\; H^{b+\infty}] \begin{Bmatrix} \phi^s \\ \phi_n^f \\ \phi^{b+\infty} \end{Bmatrix} = [G^s \;\; H^f \;\; G^{b+\infty}] \begin{Bmatrix} \mathbf{V}\cdot\mathbf{n} - \dot{w} \\ \phi^f \\ \phi_n^{b+\infty} \end{Bmatrix}, \tag{11}$$

where the superscripts s, f and $b + \infty$ indicate the boundaries defined in Figure 1.

If the structural response $\dot{w}$ in equation (11) is known, the solution for the fluid flow can then be found. As the time step progresses, the potential ϕ on the free surface and the wave elevation can be updated using equations (2) and (3). At the initial time step, ϕ on the free surface and the wave elevation are assumed to be zero.

The numerical procedure adopted here is similar to that adopted previously by others (Lin *et al.* 1985; Greenhow 1987; Wu & Eatock Taylor 1995). In fact, the linear interpolation function used here is virtually the same as that in the cited publications. The difference is that we have used a real potential rather than a complex potential, which is limited to two-dimensional flow only. Also the method used in this work to deal with the intersection point of the body and the free surface is somewhat different from that used in the complex potential theory method. Here, at the contact point, $\partial\phi/\partial n$ is discontinuous and has two values. In the calculation it is treated as known on the body surface, but unknown on the free surface. The latter is then found from the solution of equation (11). The potential at the contact point is continuous and is known from the free surface boundary condition.

A known difficulty of this problem is the jet formed during the impact. In the initial stages, before the jet is developed, the mesh structure near the intersection point is shown in Figure 3(a). As water moves continuously along the body surface, the angle between F_1F_2 and F_1P_2 becomes smaller and smaller. When the angle is below a threshold value, it is then difficult to maintain the accuracy of the results. When that happens, the first element on the

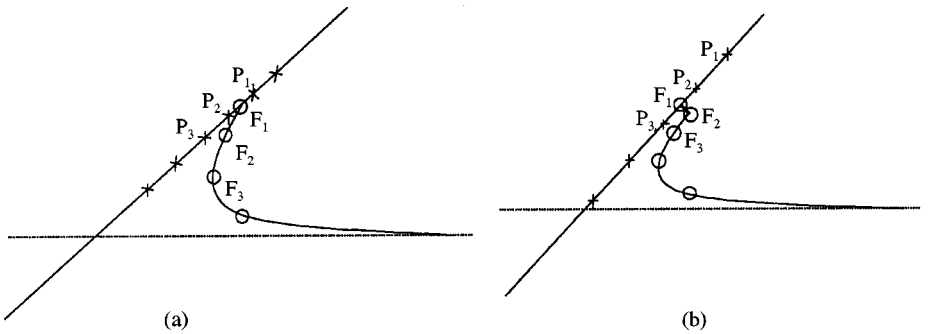

Figure 3. Sketch of grid near intersection point (F_1).

free surface, F_1F_2, will be deleted, and an extra jet element will be introduced into the calculation by moving point F_1 along the body surface, so that F_1F_2 becomes perpendicular to the body surface. The potential on F_1 is obtained by interpolation of the results on the body surface. The mesh structure after the jet has been cut is shown in Figure 3(b). Here the jet movement along the body surface is determined by the movement of point F_1. According to the numerical experiments, a suitable threshold angle should be around $\pi/20$–$\pi/60$. In our computation, we mainly cut the jet by using a maximum value of jet thickness, which means that a jet thinner than this thickness will be taken out of the calculation. A suitable jet thickness is found to be dependent on the deadrise angle. Usually, a smaller deadrise angle corresponds to a smaller maximum value. As expected, our numerical simulation suggests that a larger maximum thickness corresponds to a shorter remaining jet and a smaller thickness will lead to a longer remaining jet. A longer jet will normally give a more stable pressure distribution along the wetted body surface, and can reduce and even avoid oscillations of pressure near the intersection point as noticed by Zhao & Faltinsen (1993) and in this work. After the jet element is introduced into the calculation, if the angle between F_2F_3 and the body surface becomes smaller than the threshold value, this element will be cut in the manner described previously. If the jet is not cut, it will become longer and longer, and thinner and thinner. It will require a mesh of sufficient resolution to maintain the accuracy of the calculated results. This may be necessary if the detailed flow structure is needed within the jet. The result itself, however, has little effect on the deformation of the structure as the pressure within the jet is almost constant and is equal to atmospheric pressure.

2.2. Structural Analysis

The finite element method is used to analyse the elastic response of the structure. The plates on both sides are divided into two-node finite elements. In the local coordinate system 0_k–x_k on element k, as shown in Figure 4, the nodal displacement vector $\{\delta\}_k$ of the element can be expressed as

$$\{\delta\}_k = [w_{k1} \quad \theta_{k1} \quad w_{k2} \quad \theta_{k2}]^T, \tag{12}$$

where w_{k1}, w_{k2} are the displacements of nodes, and θ_{k1}, θ_{k2} are the angles of rotation which are positive in the clockwise direction.

The relation between the deformation curve and the nodal vector $\{\delta\}_k$ can be written as (Timoshenko *et al.* 1972)

$$w_k(x_k, t) = [H][R]\{\delta\}_k, \tag{13}$$

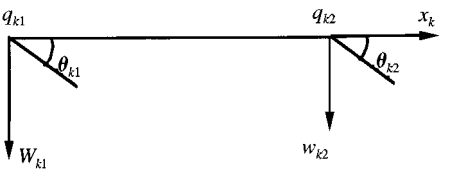

Figure 4. Structural element.

in which

$$[H] = [1 \quad x_k \quad x_k^2 \quad x_k^3] \tag{14}$$

$$[R] = \begin{bmatrix} 1 & 0 & 0 & 0 \\ 0 & 1 & 0 & 0 \\ -3/l^2 & -2/l & 3/l^2 & -1/l \\ 2/l^3 & 1/l^2 & -2/l^3 & 1/l^2 \end{bmatrix}; \tag{15}$$

from Figures 2 and 4, it is evident that $x_k = \xi - \xi_{k1}$.

It should also be pointed out that a straight line within an element is used for hydrodynamic analysis while a curve is used in the structural analysis. Strictly speaking therefore, the body surface boundary condition for the fluid flow is not exactly imposed on its surface because of the gap between the straight line and the curve. But the gap is negligibly small in reality. Thus, the error due to this apparent incompatibility is not expected to be more significant than that due to the fact the boundary condition is imposed on the nodes of the element only, rather than everywhere within the element. Both errors will of course diminish when all the elements become smaller and smaller.

The dynamic equilibrium equation of the element can be expressed as (Timoshenko *et al.* 1972)

$$[M]_k\{\ddot{\delta}\}_k + [K]_k\{\delta\}_k = \{F\}_k, \tag{16}$$

where $[M]_k$ is the element mass matrix, $[K]_k$ is the element stiffness matrix, $\{F\}_k$ is the equivalent nodal load vector of the element. $[M]_k$ and $[K]_k$can be written as

$$[M]_k = \frac{\rho h l}{420}\begin{bmatrix} 156 & 22l & 54 & -13l \\ 22l & 4l^2 & 13l & -3l^2 \\ 54 & 13l & 156 & -22l \\ -13l & -3l^2 & -22l & 4l^2 \end{bmatrix},$$

$$[K]_k = \frac{D}{l^3}\begin{bmatrix} 12 & 6l & -12 & 6l \\ 6l & 4l^2 & -6l & 2l^2 \\ -12 & -6l & 12 & -6l \\ 6l & 2l^2 & -6l & 4l^2 \end{bmatrix}, \tag{17}$$

in which ρ is the density of the structure and is assumed to be a constant, $D = Eh^3/[12(1-\mu^2)]$ is the stiffness coefficient of the plate, E is the elastic modulus, and μ is the Poisson ratio. Structural damping has been ignored in equation (16).

In the case of the impact problem, the nodal load is derived from Bernoullis equation in the hydrodynamic analysis. The expression for $\{F\}_k$ can be written as

$$\{F\}_k = [R]^{\mathrm{T}} \int_{\xi_{k1}}^{\xi_{k2}} [\mathrm{H}]^{\mathrm{T}} p_k(\xi, t)\, \mathrm{d}\xi, \tag{18}$$

in which $p_k(\xi, t)$ is the impact pressure over the kth element, and ξ_{k1} and ξ_{k2} are shown in Figure 2.

The global structural equilibrium equation can be obtained by assembling the element equilibrium equation (16),

$$[M]\{\ddot{\delta}\} + [K]\{\delta\} = \{F\} \tag{19}$$

in which $[M]$, $[K]$ and $\{F\}$ are the global mass matrix, stiffness matrix and nodal load vector, respectively. When the pressure distribution acting upon the plates is found, the structural response can be obtained by solving equation (19).

2.3. Coupled Hydroelastic Equation

The coupled hydroelastic equation can be derived from equations (11) and (16). During water entry, the hydrodynamic pressure acting upon the wetted surface can be obtained from Bernoulli's equation,

$$p = p_0 - \rho_w \left[\frac{\mathrm{d}\phi}{\mathrm{d}t} - \mathbf{V}_p \cdot \nabla\phi + \frac{1}{2} \nabla\phi \cdot \nabla\phi \right], \tag{20}$$

where ρ_w is water density, $\mathbf{V}_p$ is the velocity of point p of the body surface, and $\mathrm{d}\phi/\mathrm{d}t = (\mathrm{d}/\mathrm{d}t)\{\phi[x_p(t), y_p(t), t]\}$. The atmospheric pressure p_0 in equation (20) can be taken as zero.

In order to obtain the global coupled structural equilibrium equation, we shall first linearize the nonlinear terms in equation (20). Writing $\nabla\phi = (\phi_n, \phi_\tau)$ and $\mathbf{V}_p = (V_n, V_\tau)$, where the subscripts n and τ indicate the components in the normal and tangential directions, respectively, and applying the interpolation function in equations (5)–(20), we obtain the following expression for the pressure on the kth element:

$$\begin{aligned} -\frac{p_k}{\rho_w} &= \dot{\phi} - (V_n\phi_n + V_\tau\phi_\tau) + \frac{1}{2}(\phi_n^2 + \phi_\tau^2) \\ &= N_1\dot{\phi}_{k1} + N_2\dot{\phi}_{k2} - (N_1 V_{nk1}\phi_{nk1} + N_2 V_{nk2}\phi_{nk2}) - V_\tau \left[\frac{1}{l}(\phi_{k2} - \phi_{k1}) \right] \\ &\quad + \frac{1}{2}(N_1\phi_{nk1} + N_2\phi_{nk2})^2 + \frac{1}{2l^2}(\phi_{k2} - \phi_{k1})^2 \\ &= [N_1 \quad N_2] \begin{Bmatrix} \dot{\phi}_{k1} \\ \dot{\phi}_{k2} \end{Bmatrix} + [b_1 \quad b_2] \begin{Bmatrix} \phi_{k1} \\ \phi_{k2} \end{Bmatrix} + [c_1 \quad c_2] \begin{Bmatrix} \phi_{nk1} \\ \phi_{nk2} \end{Bmatrix}, \end{aligned} \tag{21}$$

where

$$\phi = \mathrm{d}\phi/\mathrm{d}t, \quad b_1 = \frac{1}{2l^2}(\phi_{k1} - \phi_{k2}) + \frac{1}{l}V_\tau,$$

$$b_2 = -\frac{1}{2l^2}(\phi_{k1} - \phi_{k2}) - \frac{1}{l}V_\tau, \quad c_1 = \tfrac{1}{2}N_1^2\phi_{nk1} + \tfrac{1}{2}N_1N_2\phi_{nk2} - N_1V_{nk1}, \tag{22}$$

$$c_2 = \tfrac{1}{2}N_1N_2\phi_{nk1} + \tfrac{1}{2}N_2^2\phi_{nk2} - N_2V_{nk2},$$

and the meaning of subscripts k_1 and k_2 is the same as that in equation (7). Here, the values of the potential and its normal derivatives in equation (22) are taken from the solution at the previous time step. Equation (21) then becomes linear. This procedure is somewhat similar to the semi-implicit scheme used in solving the Navier–Stokes equations.

Substituting equation (21) into equations (18) and (16) and using $V_n = \phi_n$ will produce

$$[M]_k\{\ddot{\delta}\}_e + [K]_k\{\delta\}_k = \{\lambda\}_k, \tag{23}$$

where

$$\{\lambda\}_k = -[A]_k\begin{Bmatrix}\dot{\phi}_{k1}\\ \dot{\phi}_{k2}\end{Bmatrix} - [B]_k\begin{Bmatrix}\phi_{k1}\\ \phi_{k2}\end{Bmatrix} - [C]_k\begin{Bmatrix}\phi_{nk1}\\ \phi_{nk2}\end{Bmatrix}, \tag{24}$$

and

$$[A]_k = \begin{bmatrix} 7l/20 & 3l/20 \\ l^2/20 & l^2/30 \\ 3l/20 & 7l/20 \\ -l^2/30 & -l^2/20 \end{bmatrix}, \qquad [B]_k = \begin{bmatrix} l\cdot b_1/2 & l\cdot b_2/2 \\ l^2\cdot b_1/12 & l^2 b\cdot_2/12 \\ l\cdot b_1/2 & l\cdot b_2/2 \\ -l^2\cdot b_1/12 & -l^2\cdot b_2/12 \end{bmatrix},$$

$$[C]_k = \frac{1}{120}\begin{bmatrix} l(-26\phi_{nk1} + 5\phi_{nk2}) & l(5\phi_{nk1} - 14\phi_{nk2}) \\ l^2(-4\phi_{nk1} + \phi_{nk2}) & l^2(\phi_{nk1} - 3\phi_{nk2}) \\ l(-14\phi_{nk1} + 5\phi_{nk2}) & l(5\phi_{nk1} - 26\phi_{nk2}) \\ l^2(3\phi_{nk1} - \phi_{nk2}) & l^2(-\phi_{nk1} + 4\phi_{nk2}) \end{bmatrix}. \tag{25}$$

Matrices $[A]_k$, $[B]_k$ and $[C]_k$ are generated by integrating equation (18). Assembling equation (23) and combining it with equation (11), the coupled hydroelastic equation can be written as

$$\left[\begin{array}{c|ccc} M & 0 & 0 & 0 \\ \hline 0 & 0 & 0 & 0 \end{array}\right]\begin{Bmatrix}\ddot{\delta}\\ \ddot{\phi}^s\\ \ddot{\phi}_n^f\\ \ddot{\phi}^{b+\infty}\end{Bmatrix} + \left[\begin{array}{c|ccc} -C & A & 0 & 0 \\ \hline G^s & 0 & 0 & 0 \end{array}\right]\begin{Bmatrix}\dot{\delta}\\ \dot{\phi}^s\\ \dot{\phi}_n^f\\ \dot{\phi}^{b+\infty}\end{Bmatrix}$$

$$+ \left[\begin{array}{c|ccc} K & B & 0 & 0 \\ \hline 0 & H^s & G^f & H^{b+\infty} \end{array}\right]\begin{Bmatrix}\delta\\ \phi^s\\ \phi_n^f\\ \phi^{b+\infty}\end{Bmatrix} = \left[\begin{array}{c|ccc} -C & 0 & 0 & 0 \\ \hline 0 & G^s & H^f & G^{b+\infty} \end{array}\right]\begin{Bmatrix}\mathbf{V}\cdot\mathbf{n}\\ \mathbf{V}\cdot\mathbf{n}\\ \phi^f\\ \phi_n^{b+\infty}\end{Bmatrix}, \tag{26}$$

in which matrices $[A]$, $[B]$ and $[C]$ are assembled from $[A]_k$, $[B]_k$ and $[C]_k$, respectively, and columns of zeros have also been added to ensure that the number of columns is the same as the number of rows.

The second term on the left-hand side of equation (26) indicates that the coupled structural and hydrodynamic equation will introduce a term similar to damping in the system even though the structural damping is neglected. In the calculation, the FEM for structural analysis and BEM for hydrodynamic analysis have identical element nodes on the wetted surface, while the integration in equation (18) is performed along the boundary element.

It is also worth noting that equation (26) does not contain the rows corresponding to the displacements at the ends of the plate, because they are zero, based on the boundary

condition. Also since the shear force from the ends will be present only in these rows, they will not have any contribution to equation (26).

3. NUMERICAL RESULTS

A computer program has been developed for calculating the interactive response of the structure impacting water with constant speed. In the program, equation (26) is solved by the Newmark direct integral method (Bathe & Wilson 1976).

During the impact, the intersection points G and B (see Figure 1) will move up along the body surface. At each time step, the intersection point may not always fall on the node of the boundary element. When the intersection point moves to a position within an element, the upper limit of the integration in equation (18) should be set at the intersection point beyond which the pressure is zero. As a result, changes have to be made in equation (25).

Unless specified otherwise, the parameters used in the numerical computation are as follows: length of plate $L = 0{\cdot}4$ m, speed of entry $V = 1{\cdot}0$ m/s, elastic modulus of plate $E = 200$ GPa, Poisson's coefficient of plate $v = 0{\cdot}3$, density of plate material $\rho = 7800\ \text{kg/m}^3$, density of water $\rho_w = 1000\ \text{kg/m}^3$. Symmetry about $x = 0$ is used in the calculation. The plate is divided into elements of the same length Δx. On the free surface and along the symmetry line, the element size varies. Larger elements are used away from the body to reduce the CPU requirement. The size of the element on the free surface at the intersection with the body, excluding the jet element, is set equal to that of the element on the plate. Convergence has been tested by varying these parameters (reducing the time step and the element size, and increasing the computational domain).

3.1. Validation

The FEM program for the structural analysis has been verified by comparing the calculated results with the analytical solution for the problem of dynamic response of a plate under transient rectangular impulse load, and good agreement has been found. The BEM code for hydrodynamic analysis has been used for the cases of rigid V-shaped wedges entering the water surface, with deadrise angles $\beta = 10, 20, 30, 45$ and 60°, respectively. Figures 5–9 show the comparison between the calculated results and those obtained by Zhao & Faltinsen (1993), and good agreement can be found. In these computations, the maximum jet thickness is set equal to the length of the element on the plate. From the wave profiles in these figures, it can be seen that the jet is longer than that given by Zhao & Faltisen (1993), which will help improve the results for deformation by reducing the oscillation of the pressure near the intersection. The pressure is very small within the jet and tends to zero at its tip. Zhao & Faltinsen have shown that the numerical results are in good agreement with the similarity solution (Doborav'skaya 1969) at larger deadrise angle. A difference appears at $\beta = 30^\circ$, as seen in Figure7(b), which may be due to numerical error in the similarity solution, as suggested by Zhao & Faltinsen (1993).

Figure 10 gives results for the impact of the rigid plate ($\beta = 30^\circ$), using different fluid domain sizes. The element size is set to $\Delta x = 0{\cdot}004$ m. For a domain 12 m in length by 20 m in depth, 100 elements are used on the free surface and 80 elements on the symmetry line; while for the case of $6\ \text{m} \times 10\ \text{m}$, 50 elements are used on the free surface and 40 on the symmetry line; and for the case of 3 and 5 m, 25 are used on the free surface and 20 on the symmetry line. The elements are distributed in the manner described above. The figure shows that the difference between the first and second cases is quite small, and the latter is used in the following calculation.

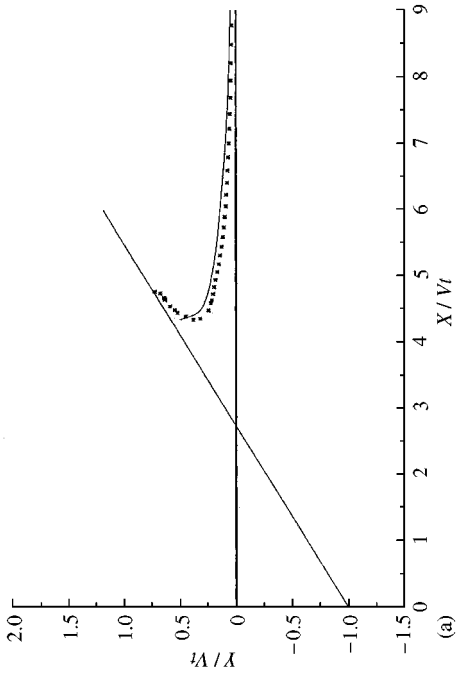

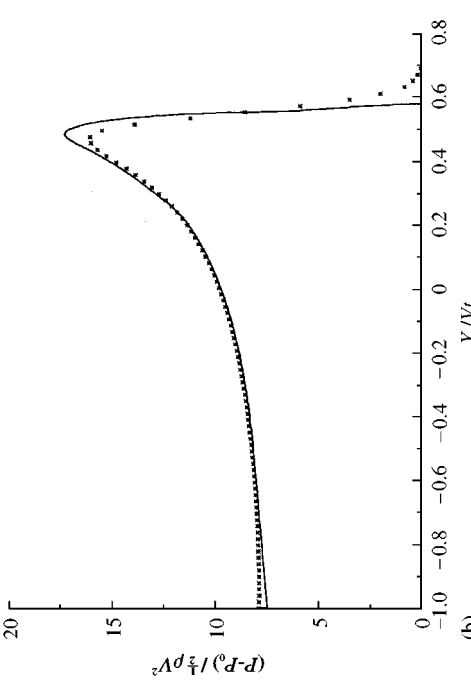

Figure 6. Results for rigid impact at $\beta = 20°$: (a) free surface profile; (b) pressure distribution. ——, Zhao & Faltinsen; * present result.

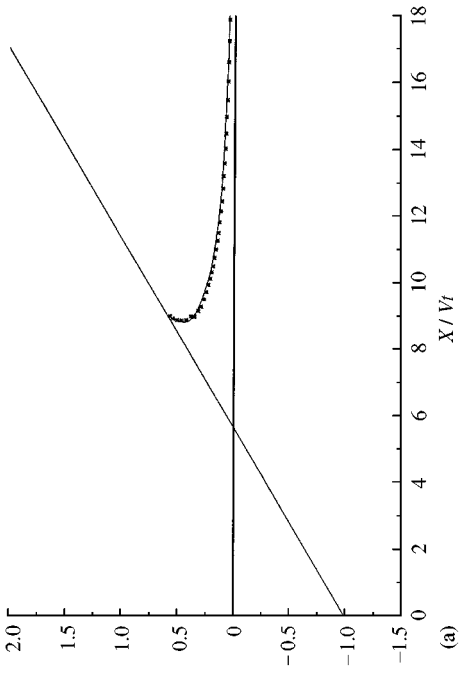

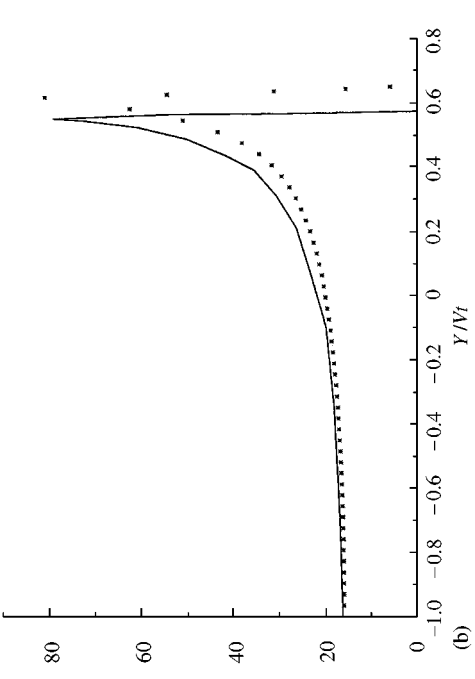

Figure 5. Results for rigid impact at $\beta = 10°$: (a) free surface profile; (b) pressure distribution. ——, Zhao & Faltinsen; * present result.

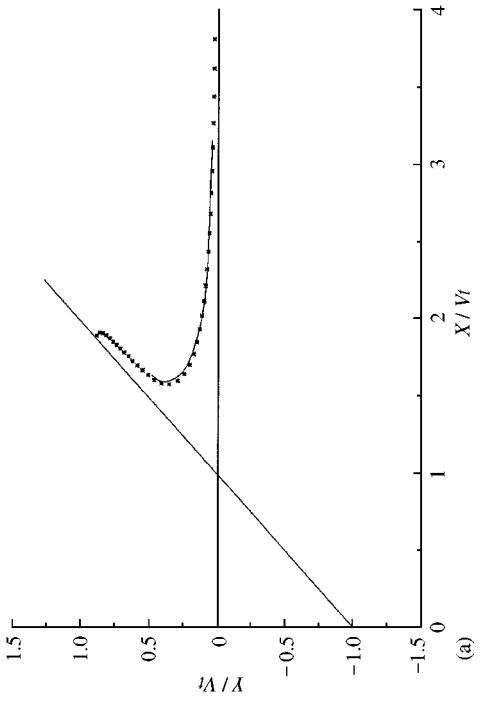

Figure 8. Results for rigid impact at $\beta = 45°$: (a) free surface profile; (b) pressure distribution. ——, Zhao & Faltinsen; * present result.

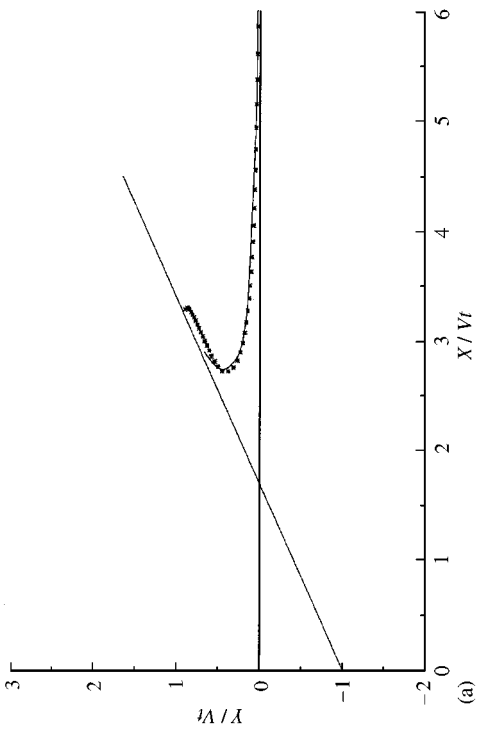

Figure 7. Results for rigid impact at $\beta = 30°$: (a) free surface profile; (b) pressure distribution. ——, Zhao & Faltinsen; * present result.

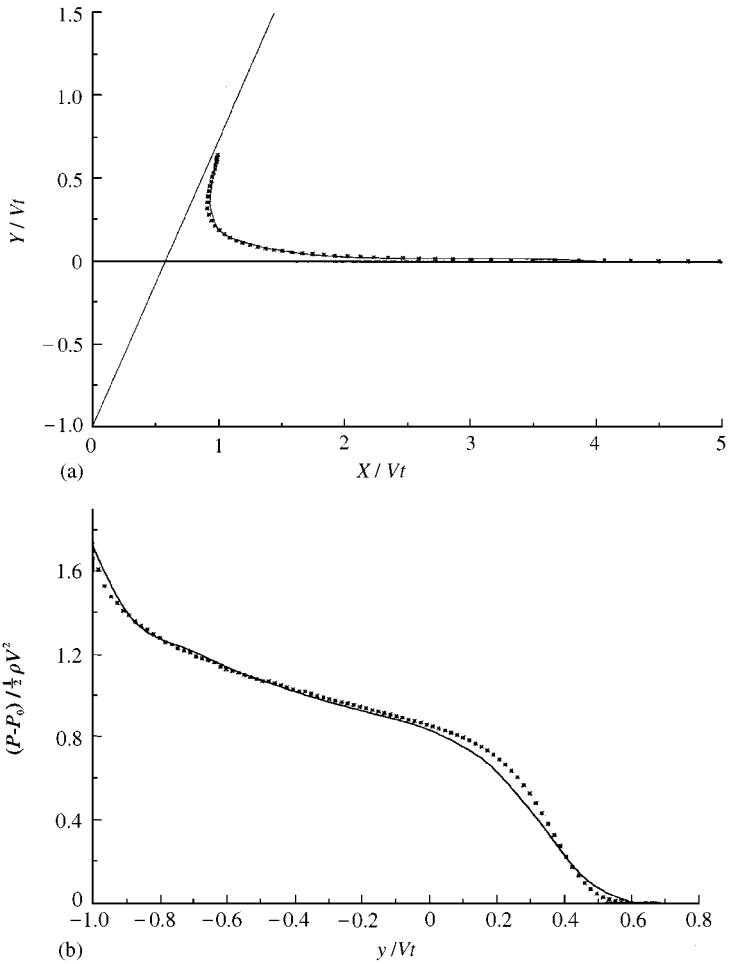

Figure 9. Results for rigid impact at $\beta = 60°$: (a) free surface profile; (b) pressure distribution. ——, Zhao & Faltinsen; $*$ present result.

Convergence with respect to mesh size is shown in Figure 11. It gives the time history of the displacement at the centre-point of the plate with $\beta = 45°$ and $h = 3$ mm. The calculation is made based on the fully coupled method shown in equation (26). The hydrodynamic pressure at the initial stage is obtained from the rigid-body solution. The interaction computation starts after a very small part of the structure has entered the water, which is to avoid processing three different boundary conditions when the tip of the wedge just touches the water. From the result, we can see that the displacement converges with the mesh size.

In order to further verify the coupled analysis, we have also developed a program based on the iterative method to calculate the hydroelastic interaction. The flowchart of the program is given in the appendix. Figure 12 gives the comparison between the results obtained from these two methods for the displacement at the mid-point of the plates with $\beta = 45°$, $h = 3$ mm and different time steps. The relative error EPS for iterative calculations in these cases is set to 1%. The figure shows that there is a noticeable difference between the result from the iterative method and that from the coupled method at $\Delta t = 0{\cdot}05$ ms.

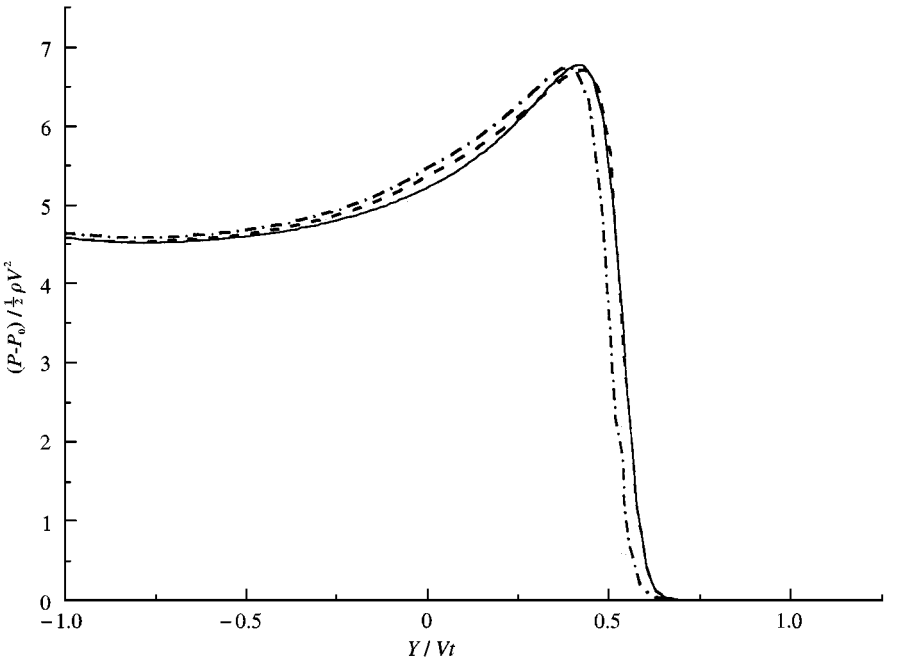

Figure 10. Convergence test with different fluid domains. ——, length = 12 m, height = 20 m; – – – –, length = 6 m, height = 10 m; -·-·-·-, length = 3 m, height = 5 m.

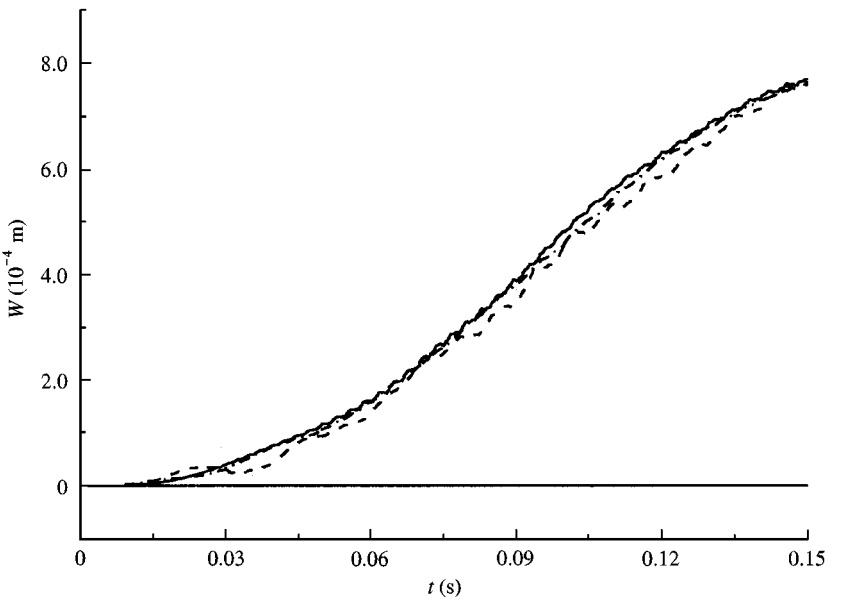

Figure 11. Convergence test with different element sizes: – – – –, $\Delta x = 0{\cdot}08$ m; -·-·-·-, $\Delta x = 0{\cdot}04$ m; ——, $\Delta x = 0{\cdot}025$ m.

The difference may be due to two reasons. One is that the coupled method is similar to the semi-implicit technique, while the iterative method corresponds to the fully implicit technique. The other reason is that the plate in this case is relatively flexible and its deformation

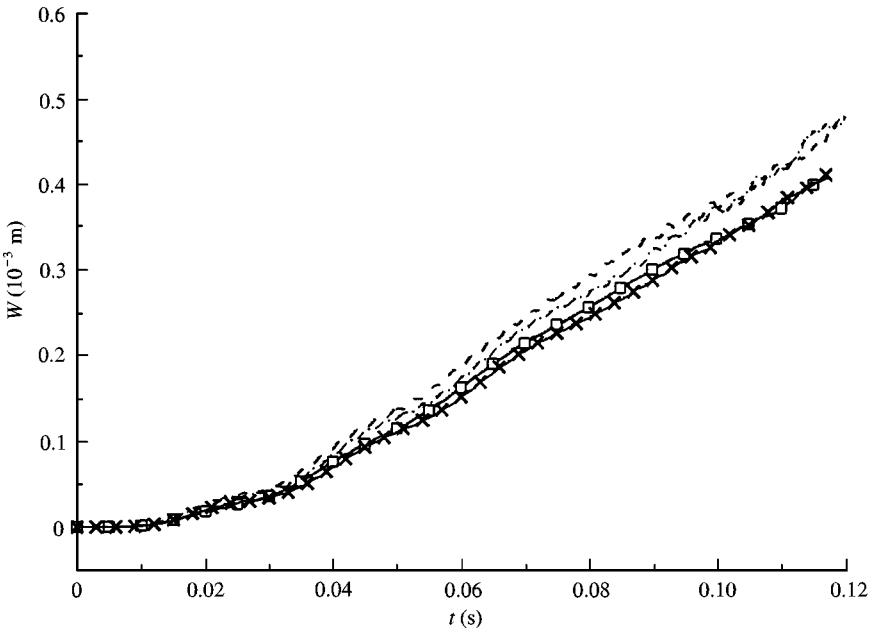

Figure 12. Convergence test with different time steps: —□—, $f = 0{\cdot}05$ s (iterative); ------, $t = 0{\cdot}05$ s (coupled); —×—, $t = 0{\cdot}01$ s (iterative); -·-·-·-, $t = 0{\cdot}01$ s (coupled).

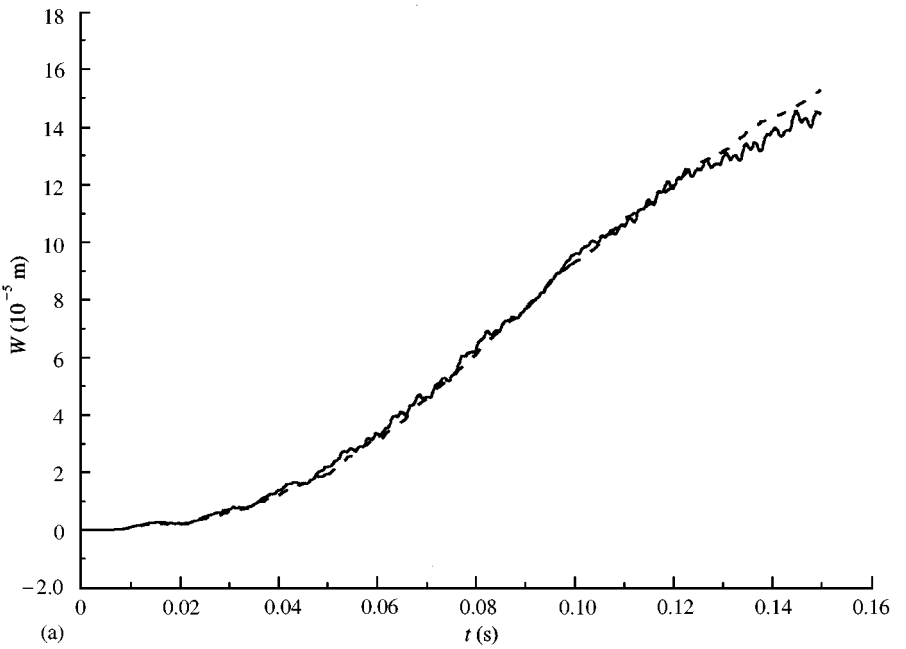

Figure 13. Middle point deformation for $\beta = 45°$: (a) $h = 5$ mm; (b) $h = 8$ mm; (c) $h = 11$ mm: ——, coupled; -----, decoupled.

is sensitive to the accuracy of the pressure calculation. A finer mesh and smaller time step is required to eliminate the difference entirely which means many days of calculation for each case and therefore such an attempt was not made in the present work. On the other hand,

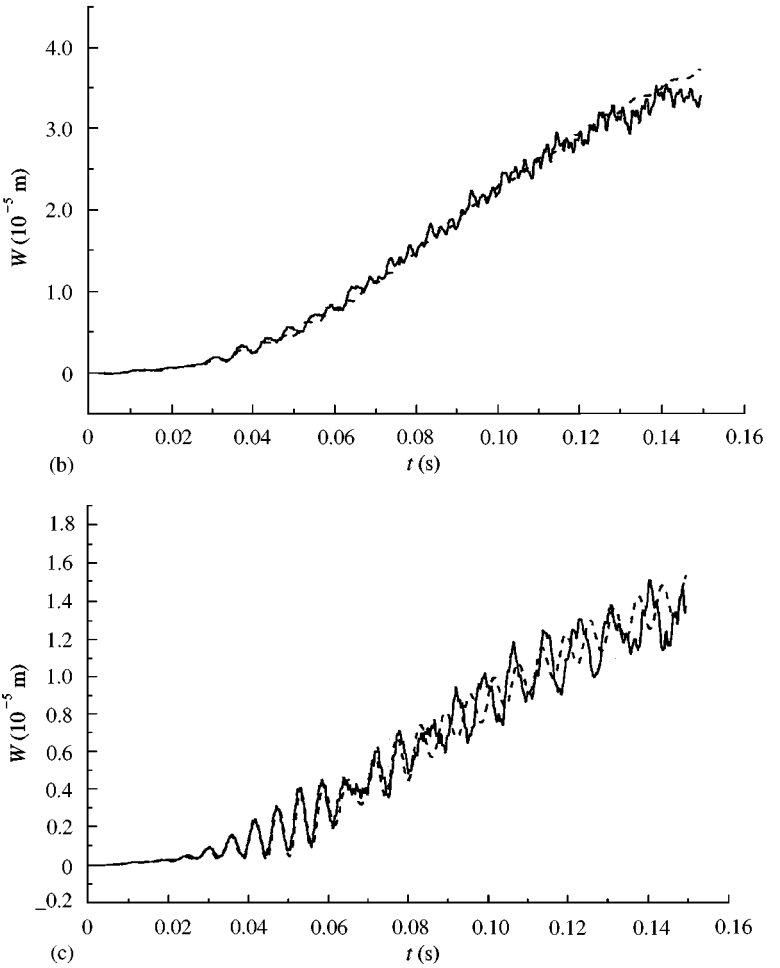

Figure 13. Continued

this figure gives the worst case observed in the calculation, and this type of difference becomes smaller, even graphically invisible, when the plate becomes thicker.

One important feature which should be highlighted here is the effect of the jet on the calculated results. As observed by Zhao & Faltinsen (1993), the pressure on the body surface oscillates sharply near the intersection. This oscillation is not physical but due to numerical inaccuracy. This unwelcome feature, however, has little effect on the results obtained by Zhao & Faltinsen for two reasons: (i) the oscillation is localized in a small area, and (ii) the pressure obtained from Bernoulli's equation does not give any feedback to the potential, and therefore the error in the pressure will not propagate into other areas or accumulate in the time domain. The situation in the present case is quite different. The oscillation in pressure will cause error in the deformation, which will further lead to numerical inaccuracy in the potential at the next time step. Thus, removing oscillations in the pressure near the intersection is essential for ensuring stable and accurate results throughout the time domain. This is mainly achieved by properly limiting the jet thickness as discussed in the last paragraph of Section 2.1. What this also means, however, is that with different time steps the jet may be cut at different instants. This clearly has implications for the convergence of the results in Figure12 with respect to time step.

3.2. Results for Different Plate Thickness and Deadrise Angle

In order to examine how important the hydroelastic coupling effect on the response of the structure is, the case of the V-shape structure with different plate thicknesses impacting water is calculated by two methods. One uses the pressure obtained from the rigid body solution and the structural and hydrodynamic analysis are therefore decoupled. The other uses the fully coupled analysis described in Section 2.3.

Figure 13 gives the comparison of results obtained from the decoupled and coupled methods for the elastic displacement at the middle point of the plate with deadrise angle $\beta = 45^\circ$ and different thicknesses. They show that the coupling effect on the displacement depends very much on the thickness of the plate. When the plate thickness becomes smaller, the difference between the displacements from the two methods is also smaller. This indicates that the coupling effect becomes relatively less significant with the decrease of the plate thickness. This is because the structural stiffness decreases sharply with thickness and the structure will be quite flexible at small thickness. As a result, the restoring force due to

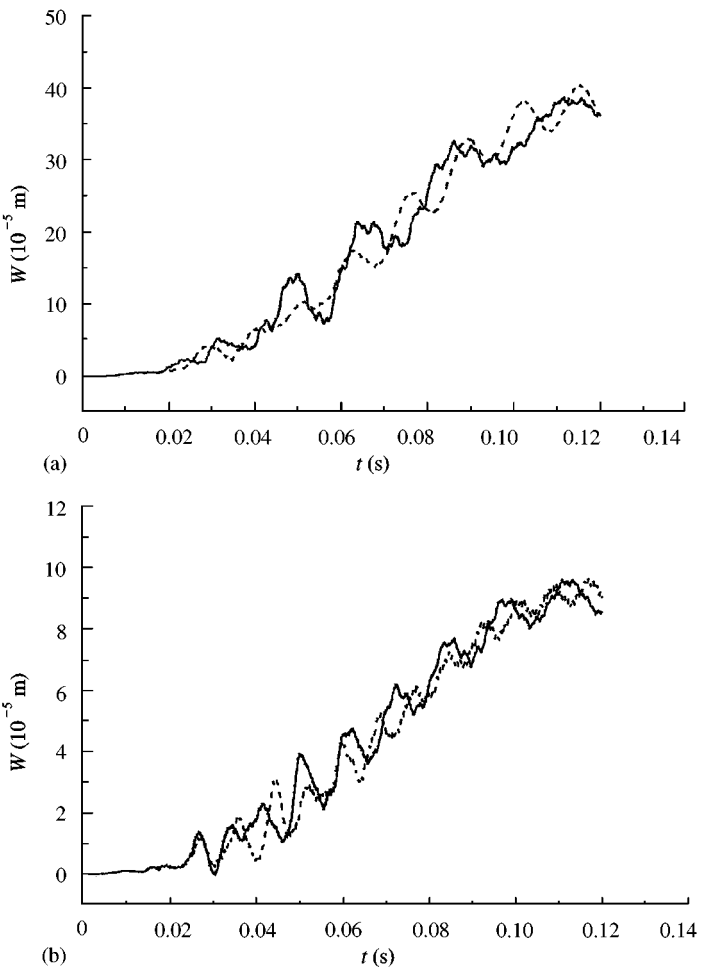

Figure 14. Middle point deformation for $\beta = 30^\circ$: (a) $h = 5$ mm; (b) $h = 8$ mm; (c) $h = 11$ mm: ——, coupled; -----, decoupled.

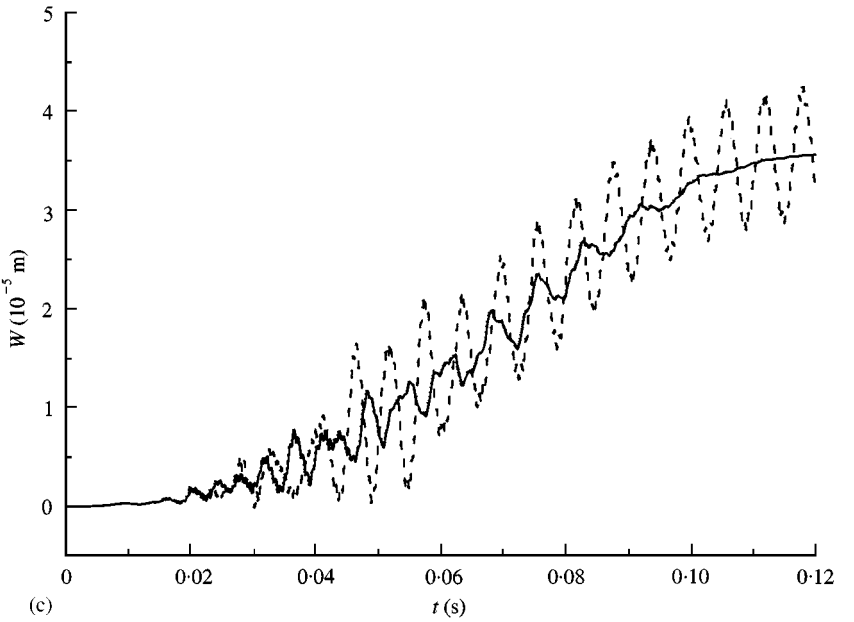

Figure 14. Continued

elastic deformation will be small and the displacement will increase until the restoring force is large enough to balance the external loading. The overall displacement of a thin plate will therefore be larger than that of a thicker plate but the coupling effect is relatively less significant. With the increase of the plate thickness, although the overall displacement becomes smaller, the coupling effect on the structural elastic response is relatively more significant, as shown in Figures 13(b) and 13(c).

Figure 14 gives the comparison of results from coupled and decoupled method for deadrise angle $\beta = 30^\circ$. They are different from those for $\beta = 45^\circ$. These figures show that, even when the plate is thin ($h = 5$ mm), the coupling effect between fluid and structure is significant. It may be due to the different pressure profiles over the structure at different deadrise angles. For $\beta = 30^\circ$, the pressure changes sharply near the jet area, but the pressure distribution for $\beta = 45^\circ$ varies very little, as seen in Figures 7 and 8.

4. CONCLUSIONS

A numerical method has been developed for the fully coupled analysis of the hydroelastic response of a structure impacting water with constant speed. The coupled equation is set up by combining the BEM-based hydrodynamic calculation and the FEM-based structural analysis. The jet flow formed during impact has been properly treated. The developed method has been verified by applying the BEM and FEM for hydrodynamic and structural analysis separately and comparing the results obtained with known data. The method is further verified by convergence tests and by comparing the results obtained from the fully coupled method with an iterative method.

Based on the cases investigated under the conditions specified in this paper, some conclusions can be drawn as follows.

(i) By introducing an extra jet element, the jet flow has been properly treated in the present numerical program. Setting a suitable maximum jet thickness can reduce oscillation

of the pressure near the intersection point. This will improve the accuracy for deformation and reduce the accumulated error in the time-domain analysis.

(ii) Fluid–structure interaction strongly affects the structural responses during impact with water. In most cases, the results from the coupled and decoupled methods are quite different. One exception is when the plate is sufficiently thin.

(iii) The method presented in this paper offers an effective tool which can be extended for the three-dimensional impact problem. However, further work, including extensive comparison with experimental data, is needed before the method is used for practical applications.

ACKNOWLEDGEMENTS

The first two authors are grateful to the Natural Science Foundation of China (NSFC) for its financial support and also appreciate Professor Lu Chuan-jing for his valuable suggestions and constructive advice. GXW is most grateful to the financial support from EPSRC (GR/K61135), U.K. The collaboration between SJTU and UCL is supported by the Royal Society and NSFC.

References

Bathe, K. J. & Wilson, E. L. 1976 *Numerical Methods in Finite Element Analysis*. Englewood Cliffs, NJ: Prentice-Hall.

Belytschko, T. & Mullen, R. 1981 Two-dimensional fluid–structure impact computation with regularization. *Computer Methods in Applied Mechanics and Engineering* **27,** 139–154.

Dobrovolskaya, Z. N. 1969 On some problems of similarity flow of fluid with a free surface. *Journal of Fluid Mechanics* **36,** 805–829.

Greenhow, M. 1987 Wedge entry into initially calm water. *Applied Ocean Research* **9,** 214–223.

Gu, M. X., Cheng, G. Y. & Zhang, X. C. 1991 Hydroelastic effects study of rotation shell with flat head during water impact. *Journal of Hydrodynamics* **6,** 42–51.

Lin, W. M., Newman, J. N. & Yue, D. K. 1985 Nonlinear force motions of floating bodies. In 15*th Symposium on Naval Hydrodynamics*, ONR, Washington, DC, U.S.A.: National Academy Press.

Lu, C. H, He, Y. S. & Wang, G. 1997 Ship hull slamming analysis by using nonlinear boundary element method. In *Proceedings of China-Korea Joint Workshop on Marine Hydrodynamics*, pp. 74–79. Shanghai: Jiao Tong University Press.

Meyerhoff, W. K. 1965 Die berechnung hydroelastischer stöße. *Schiffstechnik* **12,** 18–30 and 49–64.

Timoshenko, S., Young, D. H. & Weaver, W. Jr 1972 *Vibration Problems in Engineering*, 4th edition New York: Wiley.

Vamammoto, Y., Iida, K., Fukasawa, T., Murakami, T., Arai, M. & Ando, A. 1985 Structural damage analysis of a fast ship due to bow flare slamming, *International Shipbuilding Progress* **32,** 124–136.

Von Karman, T. 1929 The impact on seaplane floats during landing. TN 321, NACA.

WAGNER, H. 1932 Über Stoß- und Gleitvorgänge an der Oberfläche von Flüssigkeiten. *ZAMM* **12,** 193–215.

Wilkinson, J. P. D., Cappelli, A. P. & Salzman, R. N. 1968 Hydroelastic interaction of shells of revolution during water impact. *AIAA Journal* **6,** 792–797.

Wu, G. X. & Eatock Taylor, R. 1995 Time stepping solution of two dimensional nonliear wave radiation problem. *Ocean Engineering* **22,** 785–798.

Zhao, R., & Faltinsen, O. 1993 Water entry of two-dimensional bodies. *Journal of Fluid Mechanics* **246,** 593–612.

APPENDIX: THE FLOWCHART OF THE ITERATION METHOD